photonics

MDPI

Article

Photo-Switching of Protein Dynamical Collectivity

Mengyang Xu [1], Deepu George [1,*], Ralph Jimenez [2,3] and Andrea Markelz [1]

[1] Department of Physics, University at Buffalo, Buffalo, NY 14260, USA; mxu3@buffalo.edu (M.X.); amarkelz@buffalo.edu (A.M.)
[2] JILA, 440 UCB, University of Colorado, Boulder, CO 80309, USA; rjimenez@jila.colorado.edu
[3] Department of Chemistry, 215 UCB, University of Colorado, Boulder, CO 80309, USA
* Correspondence: dkgeorge@buffalo.edu

Abstract: We examine changes in the picosecond structural dynamics with irreversible photobleaching of red fluorescent proteins (RFP) mCherry, mOrange2 and TagRFP-T. Measurements of the protein dynamical transition using terahertz time-domain spectroscopy show in all cases an increase in the turn-on temperature in the bleached state. The result is surprising given that there is little change in the protein surface, and thus, the solvent dynamics held responsible for the transition should not change. A spectral analysis of the measurements guided by quasiharmonic calculations of the protein absorbance reveals that indeed the solvent dynamical turn-on temperature is independent of the thermal stability/photostate however the protein dynamical turn-on temperature shifts to higher temperatures. This is the first demonstration of switching the protein dynamical turn-on temperature with protein functional state. The observed shift in protein dynamical turn-on temperature relative to the solvent indicates an increase in the required mobile waters necessary for the protein picosecond motions, that is, these motions are more collective. Melting-point measurements reveal that the photobleached state is more thermally stable, and structural analysis of related RFP's shows that there is an increase in internal water channels as well as a more uniform atomic root mean squared displacement. These observations are consistent with previous suggestions that water channels form with extended light excitation providing O_2 access to the chromophore and subsequent fluorescence loss. We report that these same channels increase internal coupling enhancing thermal stability and collectivity of the picosecond protein motions. The terahertz spectroscopic characterization of the protein and solvent dynamical onsets can be applied generally to measure changes in collectivity of protein motions.

Keywords: protein collectivity; terahertz; thermal stability; fluorescent proteins; photobleaching

Citation: Xu, M.; George, D.; Jimenez, R.; Markelz, A. Photo-Switching of Protein Dynamical Collectivity. *Photonics* **2021**, *8*, 302. https://doi.org/10.3390/photonics8080302

Received: 16 June 2021
Accepted: 25 July 2021
Published: 29 July 2021

1. Introduction

Fluorescent proteins provide vital insight into biochemical processes. Since the discovery of green fluorescent protein (GFP) in *Aequorea victoria*, researchers have generated a large number of mutants that enable access to a rainbow of excitation and emission wavelengths. The power of these proteins is the formation of their chromophore autocatalytically from three sequential residues [1], thus enabling the incorporation of the fluorescent tag into a targeted protein's expression. All fluorescent proteins (FPs) share several structural features: an 11-stranded β-barrel with an internal distorted α-helix to which the chromophore is attached [2,3]. The chromophore removed from the protein has a poor emission yield, four orders of magnitude lower compared to when the chromophore is inside the β-barrel [4]. The β-barrel structure protects the chromophore from external quenchers and inhibits the dark state conversion through a cis to trans isomerization or light-induced protonation/deprotonation [5,6]. To achieve higher transmission through tissues, longer wavelength excitation red FPs (RFPs) have been developed. Unfortunately, the application of RFPs to imaging is limited by their higher tendency to be irreversibly photobleached. Though this photobleaching is useful for certain specialized microscopic

techniques, such as the fluorescence recovery diffusion measurements, it is more often a bottleneck for imaging applications, especially for those demanding high irradiance illuminations such as single molecule microscopy. The mechanisms that lead to this decrease in photostability are a current area of study. Here, we examine the changes in the picosecond structural dynamics of several red fluorescent proteins to see if and/or how dynamical changes may be associated with photobleaching [7,8].

Three engineered monomeric RFPs were studied: mCherry [9], mOrange2 (derivatives of DsRed from *Discosoma* sp.), and TagRFP-T (a derivative of EQFP611 from *Entacmaea quadricolor*) [5]. The structures are shown in Figure 1 [10,11], along with their relative B-factors. The B-factor, or Debye Waller factor, from the X-ray structural measurements provides a measure of the root mean squared displacement, reflecting the relative flexibility of different regions of the structure. The absolute B-factors can vary for the sample protein, due to the specifics of the experimental conditions, so to compare the B-factors among the different proteins, we normalize the B-factors to the average for the entire structure for the specific protein. These three proteins have substantially enhanced resistance to both irreversible and reversible photobleaching under different illumination conditions [12]. Techniques to characterize structural flexibility have increasingly focused on the important picosecond time scale which corresponds to librational motions of the solvent and amino acid sidechains as well as the long-range intramolecular vibrations associated with conformational change [13–16]. Here we use solution phase temperature dependent terahertz (THz) time-domain spectroscopy, which is a benchtop optical measurement with small sample size requirements that enables a systematic comparison between different mutants as a function of photoexcitation.

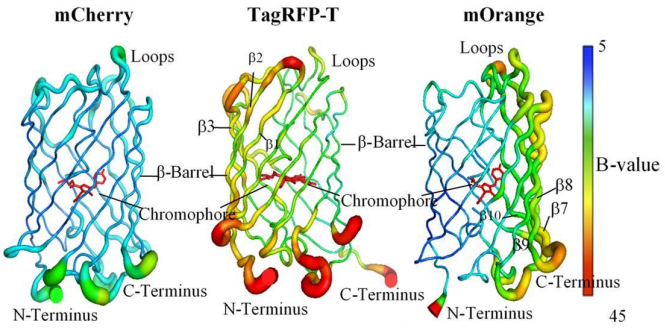

Figure 1. Structures of mCherry (2H5Q.pdb), TagRFP-T (5JVA.pdb), and mOrange (2H5O.pdb). Note that mOrange is shown as the crystal structure of mOrange2 has not been reported yet. The width and color of the ribbon in the figure show the relative atomic B-factor distribution normalized to the overall averaged B-factor value.

Comparing the THz measurements to CD measurements of thermal denaturing, the turn on temperature in THz absorbance with temperature is found to be inversely proportional to the thermal stability. Molecular modeling using quasiharmonic vibrational analysis suggests the protein dielectric response can be modeled by a Lorentzian centered at ~0.5 THz, (20 cm^{-1}, 2.5 meV). A spectral decomposition of the measured frequency dependent absorbance into the protein dielectric response and the bulk water intermolecular stretching mode at 5.3 THz (177 cm^{-1}, 22 meV) [17] shows that while the protein dynamical transition is dependent on the specific protein and photobleaching, the water has a temperature dependence that is independent of the specific RFP or its photostate. This is the first report of the protein dynamical turn-on changing independently of the solvent turn-on.

2. Materials and Methods

2.1. Sample Preparation

The RFPs were expressed and purified as discussed in Reference 12. The original concentration of the protein solution was 4 mg/mL in 15 mM MOPS buffer with 100 mM KCl at pH 7.0. It was concentrated to 80 mg/mL in the same dialysis buffer to increase the optical density at THz frequencies, using Eppendorf 5424 Microcentrifuge with Millipore Amicon 10 K centrifugal filter.

A Dolan-Jenner Fiber-Lite Illuminator light source and an Ocean Optics High Resolution Spectrometer were utilized to characterize the absorption and emission spectra. The spectral peak shifts as a function of concentration (Figure S6 in Supplementary Information). In addition, it has been verified that each sample completely loses fluorescence after 30 s under the 4 W/cm^2 532-nm illumination condition. No protein aggregation occurs in the highly concentrated solution, confirmed by the dynamical light scattering (DLS) measurements using the Zetasizer Nano ZS90 system.

2.2. THz Measurements

A conventional home-built THz time-domain spectroscopy system was employed to measure the optical absorption of RFPs within the THz range (0.2–2.2 THz) [18,19] as described in the reference [20]. In short, a home-built THz TDS system based on an 80 MHz femto-second laser and photoconductive switch was used to generate THz pulses. An electro-optic coherent detection with ZnTe as the EO crystal was employed. Time domain signal recorded were Fourier transformed to obtain the frequency domain data. A solution cell with 100-micron thick sample was placed in a gas exchange cryostat and cooled with liquid nitrogen. A silicon diode thermal sensor monitored the temperature directly adjacent to the sample aperture. After the photoactive state was measured, each sample was completely photobleached by 4 W/cm^2 532-nm illumination and at room temperature, then cooled down to 80 K for photobleached state temperature dependent measurements. The photobleaching was confirmed by monitoring the fluorescence while illuminating.

2.3. CD Measurements

Thermal stability was measured using a Jasco J-715 Spectropolarimeter for temperature dependent far-UV CD spectra. Samples were prepared at 5 μM concentration in 10 mM sodium phosphate buffer at pH 7.5 and sealed in a 10-mm path-length quartz cell. The sample was equilibrated at each temperature for 2 min, and then, 10 scans at 0.1-nm resolution were accumulated and averaged. The scan speed was set to 50 nm/min with 4 s detector response time. The temperature was gradually increased from 20 °C to 100 °C, in steps of 2 °C, using a Jasco PTC 348 WI temperature controller. The spectrum of a buffer blank was used as the reference. The melting temperatures were determined from the peak of the ellipticity temperature gradient, dθ/dT, measured at 218 nm. In the case of photobleached mCherry, the increase in the melting onset is so large that dθ/dT maximum is not yet attained by the highest temperature measured (373 K). We estimate the lower bound of the photobleached mCherry melting temperature from the midpoint between the low temperature ellipticity value and the value at the highest temperature measured, 373 K (see Figure S1).

2.4. MD Calculations

The temperature dependent absorbance spectra were calculated using quasiharmonic mode analysis and dipole autocorrelation. The MD trajectory of the net dipole was calculated with the CHARMM 39 [21] and CHARMM 36 empirical force field [22]. The special formation by the auto-oxidation and cyclization of three to four amino acid residues requires the chromophore to be additionally parameterized [23]. We applied the residue topology and parameter files for the chromophore used in Reference 23 to the calculations presented here. The initial molecular structures were obtained from the Protein Data Bank, mCherry (PDB: 2H5Q) and TagRFP-T (PDB: 3T6H). The mOrange2 structure was

obtained by modifying mOrange (PDB: 2H5O) with Q64H/F99Y/E160K/G196D mutations implemented using the CHARMM-GUI [24].

The CHARMM/TIP3P parameter set was used to model the fully solvated protein system starting from the X-ray determined structure. Each structure was first minimized at zero temperature using steepest descent method followed by the adopted basis Newton–Raphson method until the total energy gradient reached below 10^{-7} kcal Å^{-1}. The energy-minimized systems were then neutralized by adding potassium or chloride ions, randomly distributed throughout the volume.

MD simulations were performed with an integration time step of 1 fs. Each system was heated from 100 K to 300 K, with a linear gradient of 1 K/ps. The systems were equilibrated for 10 ns in the isobaric-isothermal (constant pressure-temperature, CPT) ensemble. 4-ns long production trajectories were further performed under the CPT condition at 300 K. The dipole moments about the center of geometry were obtained, and the absorption intensity was determined from the power spectra of the dipole-dipole autocorrelation function [25–27].

3. Results

In Figure 2, we show the molar absorption coefficient $\alpha(\omega,T)$ for the three RFPs at several THz frequencies for both the functional and photobleached states. Both protein and water absorption contribute to the spectra with the water dominating. Previously it has been stated that the THz absorbance follows root-mean-square-deviation (RMSD) measured by neutron scattering in the same energy range dependent on temperature and hydration. We identify two temperature regimes for the molar absorptivity: a low temperature harmonic regime (80–175 K) and a high temperature anharmonic regime (250–270 K). Below 200 K, $\alpha(\omega,T)$ increases linearly with temperature indicating that the protein vibrations in the THz range are harmonic, which is consistent with the q^2 dependent boson peak and linearly increasing RMSD shown in inelastic neutron scattering (INS) [28]. At ~200 K, the absorbance rapidly increases as the dynamics move to the anharmonic regime. The low temperature slopes differ for the three proteins, with TagRFP-T having the largest slope and mCherry the smallest. In addition, the low temperature slope decreases with photobleaching for all three RFPs. This low temperature linear regime followed by an abrupt onset in the picosecond dynamics is identical to the INS measurements of RMSD [29]. Zaccai and coworkers introduced two global flexibility parameters to quantify the RMSD temperature dependence [30]: the resilience k*, defined as proportional to the inverse of the slope of the RMSD temperature dependence at low temperatures expressed as $\langle k^* \rangle = 0.00138/(d\langle 3x^2 \rangle/dT)$, where the angular brackets denote an ensemble average over atoms and time, and the dynamical transition temperature T_D, where the dynamics sharply change. Here we take a similar approach. Assuming that the THz absorption, which selectively measures the optically active picosecond protein vibrations, is proportional to the vibrational density of states (VDOS) denoted as $g(\omega)$ which is in turn derived from the Fourier transform of the atomic velocity autocorrelation: $g(\omega) = \langle v(0)^* v(t) \rangle$ [31], we can use the harmonic approximation to express the absorption coefficient $\alpha(\omega,T)$ and $g(\omega)$ for a particular frequency ω as

$$\begin{aligned} \alpha(\omega,T) \sim g(\omega) &= \int_{-\infty}^{\infty} \langle \sqrt{m}v(0) \cdot \sqrt{m}v(t) \rangle e^{i\omega t} dt \\ &= \int_{-\infty}^{\infty} \langle \omega\sqrt{m}x(0) \cdot \omega\sqrt{m}x(t) \rangle e^{i\omega t} dt \\ &= m\omega^2 \int_{-\infty}^{\infty} \langle x(0) \cdot x(t) \rangle e^{i\omega t} dt \\ &\sim m\omega^2 \langle x^2 \rangle \sim m\omega^2 \frac{k_B T}{k^*} \\ \Longrightarrow k^* &\sim \frac{m\omega^2 k_B}{\partial\alpha(\omega,T)/\partial T} \sim \frac{C(\omega)}{\partial\alpha(\omega,T)/\partial T} \end{aligned} \quad (1)$$

where k* is an effective force constant, and C(ω) is a frequency dependent coefficient. We refer to k^* as the THz resilience. For a given frequency, we evaluate the resilience by the inverse of the slope of the molar absorptivity temperature dependence in the linear regime.

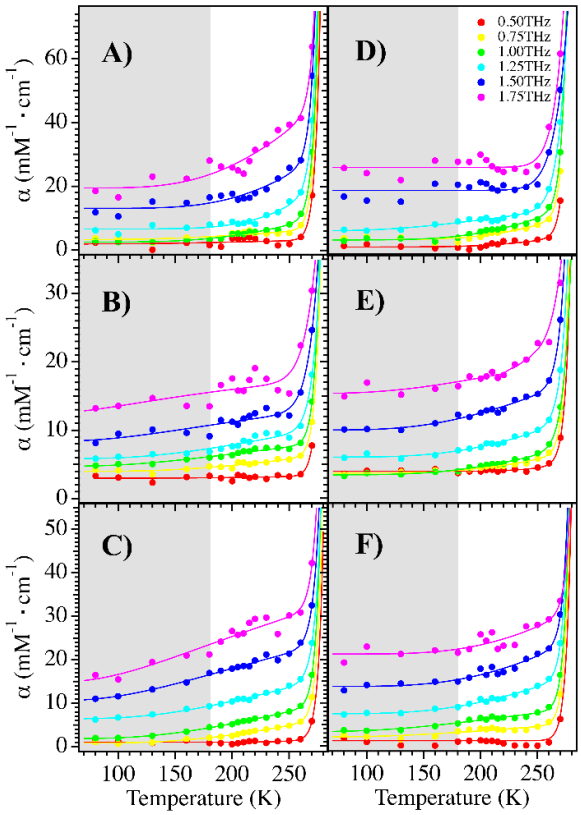

Figure 2. THz molar absorptivity for photoactive (left) and photobleached (right) RFP hydrated samples: TagRFP-T (**A**,**D**), mCherry (**B**,**E**), and mOrange2 (**C**,**F**), with interpolated lines as a guide for the eye, as a function of temperature at different frequencies. Note that vertical axis scale varies with different THz response: TagRFP-T 0–75, mCherry 0–35, mOrange2 0–55 $mM^{-1}cm^{-1}$. The low temperature region is indicated by grey shading.

In Table 1, we show the resilience extracted from the low temperature THz molar absorptivity with the measured melting temperatures (T_M) from CD measurements. The data show an increase in T_M for the photobleached state of each RFP. Strikingly, the THz resilience follows the thermal stability for all three proteins in both the unbleached and bleached states. This is the first demonstration that THz resilience correlates with thermal stability and is consistent with previous neutron scattering measurements for hemoglobins from different species [32], suggesting that stronger resilience leading to higher thermal stability may be a general phenomenon.

Table 1. The melting temperature for all samples was determined by the midpoint in the drop-off of far-UV CD signal at 218 nm. The effective force constant k^* is calculated for low temperature regime (100–200 K) at 1.0 THz, while other frequencies show similar tendency.

	mCherry	TagRFP-T	mOrange2
$T_{M,\ Unbleached}$ (K)	359 ± 2	345 ± 1	353 ± 4
$T_{M,\ Bleached}$ (K)	373 ± 2	350 ± 1	367 ± 4
$k^*_{Unbleached}$	43 ± 14	18 ± 1	21 ± 3
$k^*_{Bleached}$	45 ± 4	22 ± 3	31 ± 9

We now turn to the dynamical transition measurements which show for the first time that the protein turn-on is distinct from the solvent turn-on. The T_D seen in the THz measurements are different for the different proteins but for all three the T_D increases with photobleaching. There has been no previous report of T_D changing with the functional state of the protein and the result is unexpected. The transition has been ascribed to the slaving of protein dynamics to the solvent [33,34]. At low temperatures, the immobile water prevents large amplitude protein motions. A rapid increase in the solvent mobility at T ~200K enables the protein to access the large amplitude anharmonic motions necessary for physiological function. While the specific activation energies for the solvent motions can vary with the specific protein surface causing T_D variation protein to protein, the T_D change with photobleaching is not expected, as there is little change in the surface solvent exposure. The increase in both the T_D and T_M suggests that possibly the protein structural dynamics are playing a role in the temperature dependence. To further investigate the apparent change in the protein dynamics with photobleaching, we examine the frequency dependence of the THz absorbance for the two states. We first consider fitting the frequency dependent absorbance for a given temperature to a power law frequency dependence, $\alpha(\omega, T) \sim \omega^n$, where n is the power law factor for the temperature T. This phenomenological approach is common for characterizing the typical broadband THz absorbance for proteins [35–38]. The results in Figure 3 show that the temperature dependence of the power law substantially changes with photobleaching. For the unbleached RFP's, the power law is relatively flat below 200 K, then rapidly increases with a peak at 220 K and then drops rapidly at higher temperatures. On the other hand, the bleached RFP's is relatively flat for temperatures below 150 K, drops in value between 150 K and 200 K and then remains relatively constant above 200 K. It is clear that the picosecond dynamics have changed with bleaching.

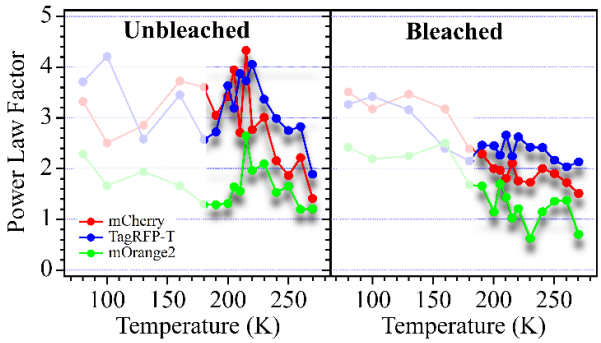

Figure 3. Power law factors from fits to THz absorption frequency dependence for unbleached (**left**) and bleached (**right**) RFP samples: mCherry (red), TagRFP-T (blue), and mOrange2 (green) as a function of temperature. The high temperature region above dynamical transition has been emphasized.

The temperature dependence of the power law fitting is obviously complex and does not provide insight into the nature of the dynamical changes, except to dramatically demonstrate these changes are present. To better resolve the source of the dynamical transition temperature shift, we isolate the protein and solvent contributions to the THz absorbance. In the case of INS measurements, the separation of the solvent dynamics from the protein dynamics is accomplished by successive measurements of protonated protein with deuterated solvent and deuterated protein with protonated solvent [39,40]. For optical measurements, ideally the isolation of different dynamics can be done using distinct spectral signatures for the protein versus solvent. At room temperature, this is not possible as protein solution THz measurements are dominated by water, which is generally modeled by the sum of three Debye terms with relaxation times of 8.3 ps, 1 ps, and 0.2 ps and an intermolecular water vibration at 5.3 THz [41–43]. The relaxational absorption is sufficiently large that intramolecular protein vibrations can be entirely neglected. At low

temperatures, however, the THz absorbance changes considerably. The THz frequency water absorption drops dramatically [44–51] as the water relaxation times increase with decreasing temperature [52] moving the relaxational water absorption loss into the MHz range, while the water intermolecular vibrational resonance [41,42], centered at 5.3 THz, remains at these lower temperatures. Thus, we can use the 5.3 THz resonance to monitor the temperature dependent solvent dynamics.

To guide our fitting of the protein contribution, we performed molecular dynamics simulations using quasiharmonic mode analysis (QHA) and dipole-dipole autocorrelation calculations. For QHA the solvent is minimized, and the harmonic approximation focuses on the collective motions of the hydrated protein only, whereas the dipole–dipole autocorrelation calculations include all motions contributing to the absorbance [25]. The VDOS and autocorrelation results are shown in Figure S2 in the Supplementary Information.

The QHA calculated isotropic absorptivity for the three RFPs below and above the T_D are shown in Figure 4. There is negligible difference among the RFPs for these calculations. The ordering in the net absorbance seen in Figure 2 is reproduced by the autocorrelation calculations however (see Figure S2 in Supplementary Information). The calculated QHA isotropic absorbance exhibits similar Lorentzian-like absorption peaks centered near 0.5 THz which become narrow and slightly shift up in frequency with increasing temperature.

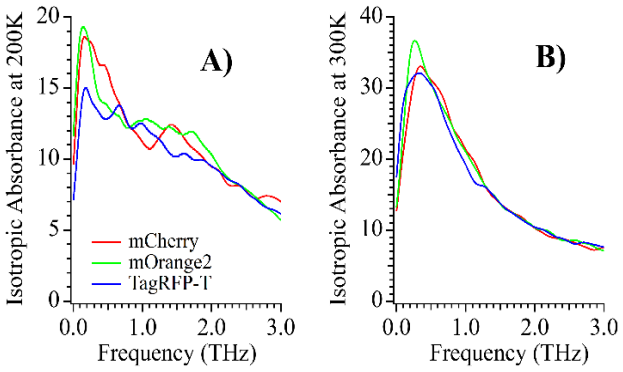

Figure 4. Isotropic THz absorption calculated by quasi-harmonic analysis at 200 K (**A**) and 300 K (**B**). High temperature absorption shows a Lorentzian-like peak centered at ~0.5 THz for all three RFPs. The same color scale is used for both plots.

Based on the QHA results, we fit our measured absorbance with two Lorentzians with one frequency set at 5.3 THz for the intermolecular water vibration. Note that only the tail of the water resonance contributes to the spectral feature as background absorption and a slight change in central frequency will not alter other fitting parameters. The results for TagRFP-T in Figure 5A,B show that the model fits the data well for the unbleached and bleached states, a substantial improvement over the simple power law fits (see Supplemental Figure S3). The different colors represent temperatures from 80 K (red) up to 275 K (purple). The full list of the temperatures is in the Supplemental Information. The jump in absorption at room temperature is due to liquid water forming due to the thawing of the solution. In Figure 6, we show the extracted resonant frequency and linewidths for the double resonant fits as a function of temperature. The temperature dependent behavior of the protein resonant band is distinctly different from the water resonance. Specifically, Figure 6A,C shows the amplitude and linewidth for the 5.3 THz water band for TagRFP-T unbleached and bleached, respectively. In both cases, the amplitude begins to rapidly decrease, and linewidth rapidly begins to increase at 200 K. The solvent transition is unaffected by the bleaching, as one might expect for the solvent dynamics. As the temperature increases, the water resonance broadens as the amplitude decreases with the net integrated intensity of the solvent intermolecular excitations remaining constant. The

broadening is consistent with additional excitations accessible with increasing thermally activated mobile waters. Figure 6B shows the frequency, amplitude, and linewidth of the low frequency band for the unbleached protein. The central frequency is nominally at 0.6 THz and blue shifts at higher temperatures, in agreement with the QHA peak in Figure 4. Both the amplitude and linewidth increase at a transition temperature of 210 K for the unbleached TagRFP-T. That is, the dynamical onset temperature for the low frequency protein motions is higher than that of the solvent. We will define two onset temperatures, from the sharp turn-on points of each curve, T_{DS} for the solvent and T_{DP} for the protein. Figure 6D shows the results for the photobleached TagRFP-T. The photobleached state T_{DP} shifts up to 230 K, while the solvent T_{DS} remains the same. mCherry has the same result (see Figure S4 in Supplementary Information). The picosecond water dynamics turn-on at 200 K for both unbleached and bleached protein, whereas the unbleached T_{DP} is 210 K and bleached is 230 K. Just as the melting temperature shifts up with bleaching, so does the turn-on for the picosecond dynamics. For mOrange2, the solvent transition is again at 200 K for both unbleached and bleached proteins. For unbleached mOrange2, the protein dynamical turn- on is again at 210 K, but the bleached mOrange2 is substantially different, with the protein dynamical transition nearly absent and a slight inflection at 220 K. In all three cases, the protein temperature dependence is not identical to the solvent.

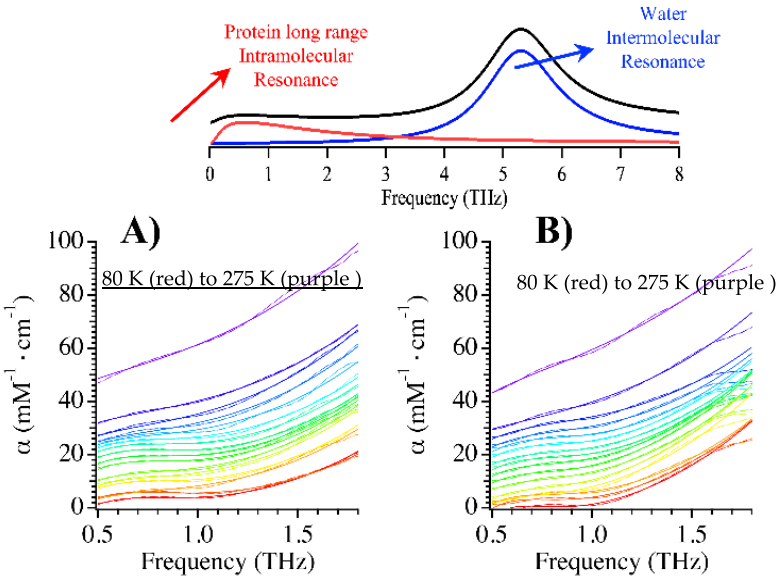

Figure 5. Comparisons of the frequency dependent THz molar absorptivity with resonance fitting lines for photoactive (**A**) and photobleached (**B**) TagRFP-T. The offset of 2 mM^{-1} cm^{-1} was applied to distinguish different temperatures, with the lowest temperature (80 K) in red and highest temperature (275 K) in purple. The top figure illustrates the decomposition of the absorption into two Lorentzian resonances: protein long-range intramolecular resonance centered at ~0.6 THz and larger-amplitude water intermolecular resonance at 5.3 THz.

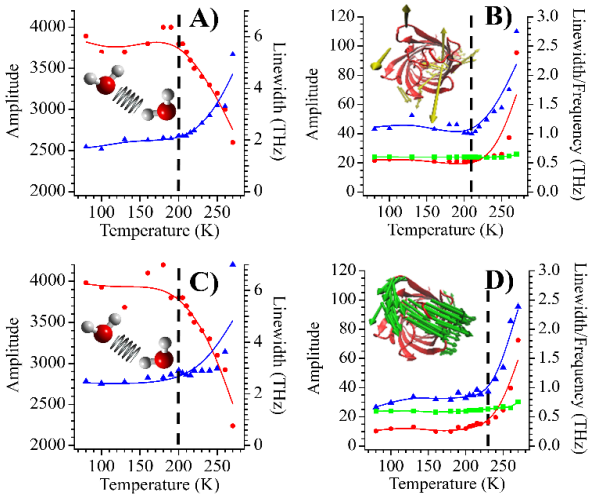

Figure 6. Resonance fitting parameters for photoactive (top) and photobleached (bottom) TagRFP-T. (**A**,**C**) Amplitude (circle, red) and linewidth (triangle, blue) corresponding to water intermolecular resonance centered at 5.3 THz. (**B**,**D**) Amplitude (circle, red), linewidth (triangle, blue), and central frequency (square, green) of the protein intramolecular resonant band; the photobleached state shows higher collectivity of the motion. The interpolated lines are used as a guide for the eye.

4. Discussion

The correlation between structural resilience and thermal stability is perhaps intuitive and consistent with previous neutron studies; however, the correlation of the protein dynamical transition temperature with thermal stability is somewhat surprising. The rapid onset in the protein dynamics with temperature has long been understood to be associated with the thermally activated motions of the surrounding solvent [33], so any trend with protein structural stability is not expected. The protein dynamical transition arises from the need to break hydrogen bonds within the solvent cage to accommodate motions. This phenomenon has been termed the slaving of the protein's dynamics to the solvent. At the same time, it is understood that the solvent excitations are influenced by the specific protein surface [34]. T_D has been observed to vary for different measurements [29,53,54] and for different proteins for a single technique [32]. For example, INS measurements using the same energy beamline for different proteins reveal onset temperatures as low as 200 K to as high as 250 K. This variation has been attributed to differences in the specific protein-solvent surface interaction [40]. The direct dependence of the protein dynamical onset on the water mobility onset appeared to be confirmed in two neutron studies where both the solvent transition and protein transition were separately measured [55,56]. For example, while T_{DS} for maltose binding protein (MBP) and hen egg white lysozyme (HEWL) are different; in both cases, the T_{DP} coincides with T_{DS}. We note that both MBP and HEWL have two lobes surrounding a binding cleft. MBP is almost entirely α-helical with a small β-sheet region at the binding site, whereas HEWL has one lobe that is mainly α-helix and the other mainly β-sheet. The picture that emerged is that for a given protein, the T_{DS} is dictated by the average solvent binding energies to the specific protein surface, and the protein structural dynamics follow the thermal activation of these surface-solvent excitations. In the results presented here, we see a somewhat extraordinary and different result where the protein dynamical turn-on clearly is different than the solvent turn-on. For each of the three proteins, the solvent T_{DS} remains essentially unchanged in the two photostates, indicating little change in the solvent–protein interactions. This is consistent with structural measurements of KillerRed and IrisFP using similar bleaching conditions [6,57]. For both KillerRed and IrisFP, there is little structural change with photobleaching. The slight decrease in THz absorbance also is consistent with the structure remaining intact, as it has been found the low temperature THz absorbance increases substantially with structural loss.

The protein dynamical onsets however are not the same as the solvent onsets and are dependent on photostate. Even in the unbleached state, T_{DP} is shifted up relative to the solvent T_{DS} for all three proteins. This difference with the previous comparisons of T_{DP} and T_{DS} for MBP and HEWL may in part arise from the more rigid β-barrel structure of the RFPs. The shift increases dramatically by 20 K with photobleaching for mCherry and TagRFP-T. This shift has not been reported previously and requires a further examination of the solvent slaving idea. As previously discussed, at low temperatures, the water motions are limited, trapping the protein configuration. As the temperature increases, water cluster motions are thermally activated, lifting the constraints on the protein dynamics. If in the measurement frequency range, the motions are highly localized, then the number of thermally activated mobile water clusters needed for the motions to occur is small, and temperature dependence of the protein dynamics will closely follow the solvent dynamical transition. Larger populations of mobile water clusters are required to execute delocalized motions, thus leading to an increase in their turn-on temperature relative to T_{DS}. In the picosecond range, it has been shown that solvent fluctuations have an Arrhenius temperature dependence [6,34,58]. We can simplistically relate the Arrhenius dependence to the thermal population of mobile waters, *N(T)*:

$$N(T) = N_{tot} e^{-\frac{E_A}{k_b T}} \tag{2}$$

where N_{tot} is the total number of waters, E_A is the activation energy, k_b is the Boltzmann constant, and T is the temperature. T_{DS} is then the temperature at which there is a sufficient high number of mobile waters to detect by THz absorbance, whereas T_{DP} indicates that the population of mobile waters necessary for the protein motions to be detectable by THz absorbance. We can define the fractional increase in the necessary mobile water population for the protein contribution as f:

$$f = \frac{N(T_{DP})}{N(T_{DS})} \tag{3}$$

Previous RMSD measurements have reported activation energies between 20–40 kJ/mol [58–64]. Using this range of activation energies and T_{DS} and T_{DP} we extract from the THz measurements, the number of mobile waters needed to detect the unbleached protein dynamics is 2–3 times the number to detect the solvent turn on, whereas for the bleached state, the number increases to 5–23 times. As there is no solvent accessible surface area (SASA) change with bleaching, this large increase in the mobile waters necessary for the picosecond protein motions contributing to the THz signal suggests that the bleached state motions are more spatially extended, with more distant regions moving in concert.

The increased collectivity of picosecond-timescale motions in the photobleached state suggested by these THz measurements is consistent with enhanced internal coupling through water channels formed by photoinduced alteration of the internal protein structure. For each of the two RFP's [6,57] whose structure has been solved in both unbleached and bleached states, under bleaching conditions similar to those used in our studies, the β-barrel structure is nearly unchanged; however, a CAVER analysis shows that additional water channels appear in the photobleached state (see Figure S5 in Supplementary Information). The dissipation of the excess energy via strong structural fluctuations provides an avenue for the water channel formation. These additional water channels can provide H-bond coupling within the β-barrel interior. The impact of the water channels on the collectivity is evident in a comparison between the CAVER water channel maps and the B-factor maps for KillerRed and IrisFP (see Figure S5 in Supplementary Information). In the photobleached state, the B-factor uniformity increases in the same regions as the water channels form. The enhanced coupling provided by the water channels is also consistent with the increase in thermal stability that we measure. Finally, we note that these same water channels likely are responsible for the loss in fluorescence in the photobleached state. All organic fluorophores, including RFPs, suffer from irreversible photobleaching after exposure to

prolonged and excessive illumination [65]. For RFPs, candidate mechanisms leading to fluorescence loss are oxidation and/or cis-trans isomerization of the chromophore [6,12,23]. Under the lower intensity illumination conditions of our study, oxidation is thought to be the dominant mechanism whereas the cis-trans isomerization mechanism occurs for more extreme conditions [66–68]. While oxygen is required for initial chromophore maturation, it has been found that photobleaching for mOrange2 and TagRFP-T is oxygen sensitive, and oxygen-free conditions result in the improved photostability [5]. Photobleaching via oxygen diffusion through the water channel in β7–β10 region in mCherry has also been discussed [23]. The presence of water channels in the photobleached state can explain an increase in dynamical collectivity, an increase in thermal stability and a loss of fluorescence by increasing oxygen access leading to trapping of the chromophore in a protonated state [57,69–71].

5. Conclusions

We find an increase in structural stability and vibrational collectivity with RFP photobleaching, consistent with enhanced intramolecular coupling via internal water channel formation with prolonged photo excitation. Both the strength of THz absorption and THz low temperature resilience correlate with thermal stability. The temperature dependent THz absorbance spectra can be used to separate the solvent and protein dynamical onsets. We find the dynamical onset of the protein motions does not coincide with that of the solvent and that it increases in the photobleached state. We suggest that the shifting of the protein dynamical onset relative to the solvent arises from the threshold mobile water population needed for the protein motions to be accessible.

Supplementary Materials: The following are available online at https://www.mdpi.com/article/10.3390/photonics8080302/s1. Figure S1: Melting Measurements of FP. Figure S2: Absorption of FP. Figure S3: Molar Absorptivity of FP. Figure S4: Temperature dependent parameter fit to THz absorption spectra. Figure S5: Debye–Waller B factor surface plots. Figure S6: Fluorescence peak of mOrange.

Author Contributions: M.X. performed THz TDS, CD, light scattering, fluorescence measurements, calculations, and analyzed data; D.G. performed THz TDS, fluorescence measurements, and analyzed data; R.J. provided samples; A.M. designed, and conceived measurements. All authors have read and agreed to the published version of the manuscript.

Funding: This research was funded by National Science Foundation MRI^2 grant DBI2959989, IDBR grant DBI1556359, MCB grant MCB1616529, the Department of Energy BES grant DE-SC0016317, and the NSF Physics Frontier Center at JILA, NSF PHY 1734006.

Data Availability Statement: The data presented in this study are available on request from the corresponding author.

Acknowledgments: The authors thank Prem P. Chapagain at Florida International University for providing RFP topology and parameter files. RJ is a staff member in the Quantum Physics Division of NIST. Certain commercial equipment, instruments, or materials are identified in this paper in order to specify the experimental procedure adequately. Such identification is not intended to imply that the materials or equipment identified are necessarily the best available for the purpose.

Conflicts of Interest: The authors declare no conflict of interest.

References

1. Tolbert, L.M.; Baldridge, A.; Kowalik, J.; Solntsev, K.M. Collapse and Recovery of Green Fluorescent Protein Chromophore Emission through Topological Effects. *Accounts Chem. Res.* **2012**, *45*, 171–181. [CrossRef] [PubMed]
2. Zimmer, M. Green fluorescent protein (GFP): Applications, structure, and related photophysical behavior. *Chem. Rev.* **2002**, *102*, 759–781. [CrossRef] [PubMed]
3. Tsien, R.Y. The Green Fluorescent Protein. *Annu. Rev. Biochem.* **1998**, *67*, 509–544. [CrossRef] [PubMed]
4. Stavrov, S.S.; Solntsev, K.M.; Tolbert, L.M.; Huppert, D. Probing the decay coordinate of the green fluorescent protein: Arrest of cis-trans isomerization by the protein significantly narrows the fluorescence spectra. *J. Am. Chem. Soc.* **2006**, *128*, 1540–1546. [CrossRef]

5. Shaner, N.C.; Lin, M.Z.; McKeown, M.R.; Steinbach, P.A.; Hazelwood, K.L.; Davidson, M.W.; Tsien, R.Y. Improving the photostability of bright monomeric orange and red fluorescent proteins. *Nat. Methods* **2008**, *5*, 545–551. [CrossRef]
6. Carpentier, P.; Violot, S.; Blanchoin, L.; Bourgeois, D. Structural basis for the phototoxicity of the fluorescent protein KillerRed. *FEBS Lett.* **2009**, *583*, 2839–2842. [CrossRef] [PubMed]
7. Kao, Y.-T.; Zhu, X.; Min, W. Protein-flexibility mediated coupling between photoswitching kinetics and surrounding viscosity of a photochromic fluorescent protein. *Proc. Natl. Acad. Sci. USA* **2012**, *109*, 3220–3225. [CrossRef]
8. Mizuno, H.; Mal, T.K.; Wälchli, M.; Kikuchi, A.; Fukano, T.; Ando, R.; Jeyakanthan, J.; Taka, J.; Shiro, Y.; Ikura, M.; et al. Light-dependent regulation of structural flexibility in a photochromic fluorescent protein. *Proc. Natl. Acad. Sci. USA* **2008**, *105*, 9227–9232. [CrossRef]
9. Shaner, N.C.; Campbell, R.E.; Steinbach, P.A.; Giepmans, B.N.G.; Palmer, A.E.; Tsien, R.Y. Improved monomeric red, orange and yellow fluorescent proteins derived from *Discosoma* sp. red fluorescent protein. *Nat. Biotechnol.* **2004**, *22*, 1567–1572. [CrossRef]
10. Shu, X.K.; Shaner, N.C.; Yarbrough, C.A.; Tsien, R.Y.; Remington, S.J. Novel chromophores and buried charges control color in mFruits. *Biochemistry* **2006**, *45*, 9639–9647. [CrossRef]
11. Liu, R.; Liang, Q.N.; Du, S.Q.; Hu, X.J.; Ding, Y. The crystal structure of red fluorescent protein TagRFP-T reveals the mechanism of its superior photostability. *Biochem. Biophys. Res. Commun.* **2016**, *477*, 229–234. [CrossRef]
12. Dean, K.M.; Lubbeck, J.L.; Binder, J.K.; Schwall, L.R.; Jimenez, R.; Palmer, A.E. Analysis of red-fluorescent proteins provides insight into dark-state conversion and photodegradation. *Biophys. J.* **2011**, *101*, 961–969. [CrossRef]
13. Niessen, K.A.; Xu, M.; Markelz, A.G. Terahertz optical measurements of correlated motions with possible allosteric function. *Biophys. Rev.* **2015**, *7*, 201–216. [CrossRef]
14. George, D.K.; Knab, J.R.; He, Y.; Kumauchi, M.; Birge, R.R.; Hoff, W.D.; Markelz, A.G. Photoactive Yellow Protein Terahertz Response: Hydration, Heating and Intermediate States. *IEEE Trans. Terahertz Sci. Technol.* **2013**, *3*, 288–294. [CrossRef]
15. Yamamoto, N.; Ohta, K.; Tamura, A.; Tominaga, K. Broadband Dielectric Spectroscopy on Lysozyme in the Sub-Gigahertz to Terahertz Frequency Regions: Effects of Hydration and Thermal Excitation. *J. Phys. Chem. B* **2016**, *120*, 4743–4755. [CrossRef] [PubMed]
16. Karplus, M.; Kuriyan, J. Molecular dynamics and protein function. *Proc. Natl. Acad. Sci. USA* **2005**, *102*, 6679–6685. [CrossRef] [PubMed]
17. Yada, H.; Nagai, M.; Tanaka, K. Origin of the fast relaxation component of water and heavy water revealed by terahertz time-domain attenuated total reflection spectroscopy. *Chem. Phys. Lett.* **2008**, *464*, 166–170. [CrossRef]
18. van Exter, M.; Fattinger, C.; Grischkowsky, D. Terahertz time-domain spectroscopy of water vapor. *Opt. Lett.* **1989**, *14*, 1128–1130. [CrossRef]
19. Wang, S.; Zhang, X.C. Pulsed terahertz tomography. *J. Phys. D Appl. Phys.* **2004**, *37*, R1. [CrossRef]
20. He, Y.; Ku, P.I.; Knab, J.R.; Chen, J.Y.; Markelz, A.G. Protein Dynamical Transition Does Not Require Protein Structure. *Phys. Rev. Lett.* **2008**, *101*, 178103. [CrossRef] [PubMed]
21. Brooks, B.R.; Bruccoleri, R.E.; Olafson, B.D.; States, D.J.; Swaminathan, S.; Karplus, M. CHARMM: A program for macromolecular energy, minimization, and dynamics calculations. *J. Comput. Chem.* **1983**, *4*, 187–217. [CrossRef]
22. Brooks, B.R.; Brooks, C.L.; MacKerell, A.D.; Nilsson, L.; Petrella, R.J.; Roux, B.; Won, Y.; Archontis, G.; Bartels, C.; Boresch, S.; et al. CHARMM: The Biomolecular Simulation Program. *J. Comput. Chem.* **2009**, *30*, 1545–1614. [CrossRef] [PubMed]
23. Chapagain, P.P.; Regmi, C.K.; Castillo, W. Fluorescent protein barrel fluctuations and oxygen diffusion pathways in mCherry. *J. Chem. Phys.* **2011**, *135*, 235101. [CrossRef]
24. Jo, S.; Kim, T.; Iyer, V.G.; Im, W. CHARMM-GUI: A web-based graphical user interface for CHARMM. *J. Comput. Chem.* **2008**, *29*, 1859–1865. [CrossRef]
25. He, Y.; Chen, J.; Knab, J.; Zheng, W.; Markelz, A. Evidence of Protein Collective Motions on the Picosecond Timescale. *Biophys. J.* **2011**, *100*, 1058–1065. [CrossRef]
26. Ding, T.; Middelberg, A.P.J.; Huber, T.; Falconer, R.J. Far-infrared spectroscopy analysis of linear and cyclic peptides, and lysozyme. *Vib. Spectrosc.* **2012**, *61*, 144–150. [CrossRef]
27. Heyden, M.; Tobias, D.J.; Matyushov, D.V. Terahertz absorption of dilute aqueous solutions. *J. Chem. Phys.* **2012**, *137*, 235103. [CrossRef]
28. Nakagawa, H.; Joti, Y.; Kitao, A.; Kataoka, M. Hydration Affects Both Harmonic and Anharmonic Nature of Protein Dynamics. *Biophys. J.* **2008**, *95*, 2916–2923. [CrossRef]
29. Doster, W.; Cusack, S.; Petry, W. Dynamical transition of myoglobin revealed by inelastic neutron scattering. *Nature* **1989**, *337*, 754–756. [CrossRef]
30. Zaccai, G. How soft is a protein? A protein dynamics force constant measured by neutron scattering. *Science* **2000**, *288*, 1604–1607. [CrossRef]
31. Heyden, M.; Tobias, D.J. Spatial Dependence of Protein-Water Collective Hydrogen-Bond Dynamics. *Phys. Rev. Lett.* **2013**, *111*, 218101. [CrossRef]
32. Stadler, A.M.; Garvey, C.J.; Bocahut, A.; Sacquin-Mora, S.; Digel, I.; Schneider, G.J.; Natali, F.; Artmann, G.M.; Zaccai, G. Thermal fluctuations of haemoglobin from different species: Adaptation to temperature via conformational dynamics. *J. R. Soc. Interface* **2012**, *9*, 2845–2855. [CrossRef] [PubMed]

33. Doster, W. The dynamical transition of proteins, concepts and misconceptions. *Eur. Biophys. J.* **2008**, *37*, 591–602. [CrossRef] [PubMed]
34. Chen, G.; Fenimore, P.W.; Frauenfelder, H.; Mezei, F.; Swenson, J.; Young, R.D. Protein fluctuations explored by inelastic neutron scattering and dielectric relaxation spectroscopy. *Philos. Mag.* **2008**, *88*, 3877–3883. [CrossRef]
35. Kawaguchi, S.; Kambara, O.; Shibata, M.; Kandori, H.; Tominaga, K. Low-frequency dynamics of bacteriorhodopsin studied by terahertz time-domain spectroscopy. *Phys. Chem. Chem. Phys.* **2010**, *12*, 10255–10262. [CrossRef]
36. Yamamoto, K.; Tominaga, K.; Sasakawa, H.; Tamura, A.; Murakami, H.; Ohtake, H.; Sarukura, N. Terahertz Time-Domain Spectroscopy of Amino Acids and Polypeptides. *Biophys. J.* **2005**, *89*, L22–L24. [CrossRef]
37. Perticaroli, S.; Nickels, J.D.; Ehlers, G.; Sokolov, A.P. Rigidity, Secondary Structure, and the Universality of the Boson Peak in Proteins. *Biophys. J.* **2014**, *106*, 2667–2674. [CrossRef]
38. Mori, T.; Jiang, Y.; Fujii, Y.; Kitani, S.; Mizuno, H.; Koreeda, A.; Motoji, L.; Tokoro, H.; Shiraki, K.; Yamamoto, Y.; et al. Detection of boson peak and fractal dynamics of disordered systems using terahertz spectroscopy. *Phys. Rev. E* **2020**, *102*, 022502. [CrossRef]
39. Schirò, G.; Fichou, Y.; Gallat, F.-X.; Wood, K.; Gabel, F.; Moulin, M.; Härtlein, M.; Heyden, M.; Colletier, J.-P.; Orecchini, A.; et al. Translational diffusion of hydration water correlates with functional motions in folded and intrinsically disordered proteins. *Nat. Commun.* **2015**, *6*, 6490. [CrossRef]
40. Wood, K.; Frölich, A.; Paciaroni, A.; Moulin, M.; Härtlein, M.; Zaccai, G.; Tobias, D.J.; Weik, M. Coincidence of Dynamical Transitions in a Soluble Protein and Its Hydration Water: Direct Measurements by Neutron Scattering and MD Simulations. *J. Am. Chem. Soc.* **2008**, *130*, 4586–4587. [CrossRef]
41. Møller, U.; Cooke, D.G.; Tanaka, K.; Jepsen, P.U. Terahertz reflection spectroscopy of Debye relaxation in polar liquids [Invited]. *J. Opt. Soc. Am. B* **2009**, *26*, A113–A125. [CrossRef]
42. Penkov, N.; Shvirst, N.; Yashin, V.; Fesenko, E.; Fesenko, E. Terahertz Spectroscopy Applied for Investigation of Water Structure. *J. Phys. Chem. B* **2015**, *119*, 12664–12670. [CrossRef]
43. Vinh, N.Q.; Sherwin, M.S.; Allen, S.J.; George, D.K.; Rahmani, A.J.; Plaxco, K.W. High-precision gigahertz-to-terahertz spectroscopy of aqueous salt solutions as a probe of the femtosecond-to-picosecond dynamics of liquid water. *J. Chem. Phys.* **2015**, *142*, 164502. [CrossRef]
44. Twardowski, J.; Anzenbacher, P.; Masson, M.R. *Raman and IR Spectroscopy in Biology and Biochemistry*; Ellis Horwood: Chichester, UK, 1994.
45. Genzel, L.; Kremer, F.; Poglitsch, A.; Bechtold, G. Relaxation processes on a picosecond time scale in hemoglobin and poly(L-alanine) observed by millimeter-wave spectroscopy. *Biopolymers* **1983**, *22*, 1715–1729. [CrossRef]
46. Genzel, L.; Santo, L.; Shen, S.C. Far-Infrared Spectroscopy of Biomolecules. In *Spectroscopy of Biological Molecules: Theory and Applications—Chemistry, Physics, Biology, and Medicine*; Sandorfy, C., Theophanides, T., Eds.; Springer: Dordrecht, The Netherlands, 1984; pp. 609–619.
47. Poglitsch, A.; Kremer, F.; Genzel, L. Picosecond relaxations in hydrated lysozyme observed by mm-wave spectroscopy. *J. Mol. Biol.* **1984**, *173*, 137–142. [CrossRef]
48. Powell, J.W.; Edwards, G.S.; Genzel, L.; Kremer, F.; Wittlin, A.; Kubasek, W.; Peticolas, W. Investigation of far-infrared vibrational modes in polynucleotides. *Phys. Rev. A* **1987**, *35*, 3929–3939. [CrossRef]
49. Powell, J.W.; Peticolas, W.L.; Genzel, L. Observation of the far-infrared spectrum of five oligonucleotides. *J. Mol. Struct.* **1991**, *247*, 107–118. [CrossRef]
50. Wittlin, A.; Genzel, L.; Kremer, F.; Häseler, S.; Poglitsch, A.; Rupprecht, A. Far-infrared spectroscopy on oriented films of dry and hydrated DNA. *Phys. Rev. A* **1986**, *34*, 493–500. [CrossRef] [PubMed]
51. Zakaria, H.A.; Fischer, B.M.; Bradley, A.P.; Jones, I.; Abbott, D.; Middelberg, A.P.; Falconer, R.J. Low-frequency spectroscopic analysis of monomeric and fibrillar lysozyme. *Appl. Spectrosc.* **2011**, *65*, 260–264. [CrossRef]
52. Kaatze, U. Complex permittivity of water as a function of frequency and temperature. *J. Chem. Eng. Data* **1989**, *34*, 371–374. [CrossRef]
53. Stadler, A.M.; Digel, I.; Embs, J.P.; Unruh, T.; Tehei, M.; Zaccai, G.; Buldt, G.; Artmann, G.M. From powder to solution: Hydration dependence of human hemoglobin dynamics correlated to body temperature. *Biophys. J.* **2009**, *96*, 5073–5081. [CrossRef]
54. Frolov, E.N.; Gvosdev, R.; Goldanskii, V.I.; Parak, F.G. Differences in the dynamics of oxidized and reduced cytochrome c measured by Mössbauer spectroscopy. *JBIC J. Biol. Inorg. Chem.* **1997**, *2*, 710–713. [CrossRef]
55. Paciaroni, A.; Orecchini, A.; Cornicchi, E.; Marconi, M.; Petrillo, C.; Haertlein, M.; Moulin, M.; Sacchetti, F. Coupled thermal fluctuations of proteins and protein hydration water on the picosecond timescale. *Philos. Mag.* **2008**, *88*, 4071–4077. [CrossRef]
56. Chen, S.-H.; Liu, L.; Fratini, E.; Baglioni, P.; Faraone, A.; Mamontov, E. Observation of fragile-to-strong dynamic crossover in protein hydration water. *Proc. Natl. Acad. Sci. USA* **2006**, *103*, 9012–9016. [CrossRef] [PubMed]
57. Duan, C.; Adam, V.; Byrdin, M.; Ridard, J.; Kieffer-Jaquinod, S.; Morlot, C.; Arcizet, D.; Demachy, I.; Bourgeois, D. Structural Evidence for a Two-Regime Photobleaching Mechanism in a Reversibly Switchable Fluorescent Protein. *J. Am. Chem. Soc.* **2013**, *135*, 15841–15850. [CrossRef] [PubMed]
58. Doster, W. The protein-solvent glass transition. *Biochim. Biophys. Acta Proteins Proteom.* **2010**, *1804*, 3–14. [CrossRef]
59. Bragger, J.M.; Dunn, R.V.; Daniel, R.M. Enzyme activity down to-100 degrees C. *Biochim. Biophys. Acta Protein Struct. Molec. Enzym.* **2000**, *1480*, 278–282. [CrossRef]

60. Malardier-Jugroot, C.; Head-Gordon, T. Separable cooperative and localized translational motions of water confined by a chemically heterogeneous environment. *Phys. Chem. Chem. Phys.* **2007**, *9*, 1962–1971. [CrossRef] [PubMed]
61. Shinyashiki, N.; Yamamoto, W.; Yokoyama, A.; Yoshinari, T.; Yagihara, S.; Kita, R.; Ngai, K.L.; Capaccioli, S. Glass Transitions in Aqueous Solutions of Protein (Bovine Serum Albumin). *J. Phys. Chem. B* **2009**, *113*, 14448–14456. [CrossRef]
62. Schiro, G.; Caronna, C.; Natali, F.; Cupane, A. Direct Evidence of the Amino Acid Side Chain and Backbone Contributions to Protein Anharmonicity. *J. Am. Chem. Soc.* **2010**, *132*, 1371–1376. [CrossRef] [PubMed]
63. Fenimore, P.W.; Frauenfelder, H.; McMahon, B.H.; Young, R.D. Proteins are paradigms of stochastic complexity. *Phys. A* **2005**, *351*, 1–13. [CrossRef]
64. Fenimore, P.W.; Frauenfelder, H.; McMahon, B.H.; Young, R.D. Bulk-solvent and hydration-shell fluctuations, similar to alpha- and beta-fluctuations in glasses, control protein motions and functions. *Proc. Natl. Acad. Sci. USA* **2004**, *101*, 14408–14413. [CrossRef]
65. Schenk, A.; Ivanchenko, S.; Röcker, C.; Wiedenmann, J.; Nienhaus, G.U. Photodynamics of Red Fluorescent Proteins Studied by Fluorescence Correlation Spectroscopy. *Biophys. J.* **2004**, *86*, 384–394. [CrossRef]
66. Bell, A.F.; Stoner-Ma, D.; Wachter, R.M.; Tonge, P.J. Light-driven decarboxylation of wild-type green fluorescent protein. *J. Am. Chem. Soc.* **2003**, *125*, 6919–6926. [CrossRef]
67. Liu, Y.; Kim, H.R.; Heikal, A.A. Structural basis of fluorescence fluctuation dynamics of green fluorescent proteins in acidic environments. *J. Phys. Chem. B* **2006**, *110*, 24138–24146. [CrossRef] [PubMed]
68. Habuchi, S.; Cotlet, M.; Gensch, T.; Bednarz, T.; Haber-Pohlmeier, S.; Rozenski, J.; Dirix, G.; Michiels, J.; Vanderleyden, J.; Heberle, J.; et al. Evidence for the isomerization and decarboxylation in the photoconversion of the red fluorescent protein DsRed. *J. Am. Chem. Soc.* **2005**, *127*, 8977–8984. [CrossRef] [PubMed]
69. Jiménez-Banzo, A.; Nonell, S.; Hofkens, J.; Flors, C. Singlet Oxygen Photosensitization by EGFP and its Chromophore HBDI. *Biophys. J.* **2008**, *94*, 168–172. [CrossRef]
70. Jimenez-Banzo, A.; Ragas, X.; Abbruzzetti, S.; Viappiani, C.; Campanini, B.; Flors, C.; Nonell, S. Singlet oxygen photosensitisation by GFP mutants: Oxygen accessibility to the chromophore. *Photochem. Photobiol. Sci.* **2010**, *9*, 1336–1341. [CrossRef]
71. Vegh, R.B.; Bravaya, K.B.; Bloch, D.A.; Bommarius, A.S.; Tolbert, L.M.; Verkhovsky, M.; Krylov, A.I.; Solntsev, K.M. Chromophore Photoreduction in Red Fluorescent Proteins Is Responsible for Bleaching and Phototoxicity. *J. Phys. Chem. B* **2014**, *118*, 4527–4534. [CrossRef]